A battle against arsenic toxicity by Earth's earliest complex life forms

Anna El Khoury[1,2], Andrea Somogyi[2], Ernest Chi Fru[3], Farid Saleh[4]*, Ibtissam Chraiki[1], Claude Fontaine[1], Jérémie Aubineau[5], Claire Rollion-Bard[6], Mathias Harzhauser[7], Abderrazak El Albani[1]*

[1]Université de Poitiers, IC2MP, UMR 7285, CNRS, 86073 Poitiers, France
[2]NANOSCOPIUM beamline, Synchrotron SOLEIL, 91190, Saint-Aubin, France
[3]Cardiff University, School of Earth and Ocean Sciences, CF10 3AT Cardiff, United Kingdom
[4]University of Lausanne, Institute of Earth Sciences, Géopolis, CH-1015 Lausanne, Switzerland
[5]Géosciences Environnement Toulouse (GET), UMR 5563 CNRS, UR 234 IRD, UM 97 UT, CNES, Observatoire Midi-Pyrénées, 31400 Toulouse, France
[6]Université Paris-Saclay, Laboratoire des Sciences du Climat et de l'Environnement (LSCE), CNRS, CEA, UVSQ, 91191 Gif-sur-Yvette, France
[7]Natural History Museum Vienna, Geological-Palaeontological Department, Burgring 7, 1010 Vienna, Austria

***Corresponding authors**
A. El Albani: abder.albani@univ-poitiers.fr
F. Saleh: farid.nassim.saleh@gmail.com

This PDF file includes:
Supplementary Text
Figs. S1 to S9
References

Supplementary Text

1- Geological Setting

The Francevillian basin (Fig. S1), formed during the Paleoproterozoic, ~2.1 Ga, is located in the Republic of Gabon in western equatorial Africa. This basin consists of several lithostratigraphic formations, designated as Francevillian (F) FA to FE, which rest unconformably on Archean basement rocks[1]. The rocks are suitable for our study because they have been subjected to only minimal tectonic deformation and show no evidence of metamorphic alteration[2–4]. The FA Formation primarily comprises fluviatile and deltaic sandstones but also contains mudstone[5]. At its top, it contains uranium enrichments and the notable Oklo natural nuclear reactors[6]. The FB Formation is composed mainly of marine sediments deposited below storm wave base and is further subdivided lithologically into the FB1 and FB2 members with the FB1 Member divided into the FB1a-c and FB2a-c units. In this scheme, the FB1a-b units consist of interlayered shales, sandstones, and conglomerates that transition into predominantly shales at the top while the FB1c unit consists primarily of shales, with a thin iron formation overlain by black shales and a manganese-rich interval. The FB2a unit includes sandstone beds deposited during sea level fall[7]. This unit is sharply overlain by the FB2b unit, characterized by finely laminated black shales interbedded with thin siltstone layers deposited by waning storm surges. This unit contains remarkable specimens that are completely to partially pyritized and non-pyritized macrofossils belonging to three categories of pyritized specimens (including lobate and string-like forms), non-pyritized circular disks on shale surfaces and rounded aggregates of disk-shaped or flattened globular structures[8] found abundantly in the black shales. The fossil abundance decreases towards the top of the section, where silty and sandy beds are more common. In the fossiliferous quarry, the FB2b black shales are 5 meters thick and were deposited in a quiet, low-energy marine environment from a fully oxygenated water column[9]. The FC Formation is dominated by dolomites and stromatolitic cherts, indicative of shallow-water depositional conditions. Stromatolites are found on topographic highs at its base[10]. Finally, the FD Formation corresponds to black shales deposited during a transgressive phase, while the FE Formation has been predominantly eroded across the basin.

2- Indicators of hydrothermal activity

The Fe/Ti versus Al/(Al + Fe + Mn) values for the different Formations of the Francevillian section indicate that the FB1c unit and the FC Formation were deposited in an environment influenced by hydrothermal activity (low Al/(Al + Fe + Mn) values and high Fe/Ti values) compared to other Francevillian formations (Fig. 1a). All other samples show a global trend indicating a detrital source. See Chi Fru et al.[11], for a detailed examination of this proxy and its implications for hydrothermal activity and nutrient enrichment across the Francevillian sub-basin.

3- Lithostratigraphic enrichment of major elements and arsenic

The distribution of major elements in the Francevillian section are presented in Table S1. In the FA Formation, SiO_2, Al_2O_3 and TiO_2 concentrations (wt.%) (Fig. S9) reflect the different lithologies, illustrated by elevated concentrations of SiO_2 and low concentrations of Al_2O_3 and TiO_2 in the sandstone. This contrast with the geochemical compositions of mudstone samples located in the upper part of the Fa Formation as previously described in Bankole et al.[5]. The FB1a unit displays the same fluctuation path as the Fa mudstone, while a decrease in Al_2O_3 and an increase then a decrease of Na_2O upsection (Fig. S9) was noticed in the FB2a unit. In the FB1c unit, as previously reported in Chi Fru et al.[11], the thin iron formation is illustrated by enrichments in Fe_2O_3, P_2O_3 and K_2O (Fig. S9), while the Mn-carbonates are highlighted by an exclusive increase in MnO and CaO (Fig. S9). Moving to the FB2a unit, the major elements distributions reflect the lithology with sandstone at the base and shale in the upper part just before the FB2b black shales, rich in the eukaryotic macrofossils. In this unit, some samples are enriched in Na_2O compared to others (Fig. S9), while the other elements follow the global tendency of the previous unit. The FC Formation, composed of cherts, dolostones and black shales, manifests diverse enrichment in SiO_2, Al_2O_3, MgO and CaO (Fig. S9) due to the presence of different rocks. The FD Formation, composed mainly of black shales, shows a geochemical composition of major elements similar to that of the FB2b unit of black shales.

Arsenic is either absent or undetectable in the FA Formation and lowest part of the FB Formation (FB1a unit) (Table S1). A progressive increase is noticeable upsection with an average of 4.36 ppm in the FB1b unit. In the FB1c unit, the As concentration still increases with an average of 22.5 ppm with some samples showing As content of up 156 ppm. Then, a decrease in As concentration is observed in the FB2a and FB2b samples, averaging 4.93 ppm and 8.47ppm, respectively. The FC formation shows higher As concentration relative to the FB2b Member with an average of 23.55 ppm. As concentration in the FD Formation displays the highest values with an average of 70.32 ppm. The As enrichment factor values indicate that As is weakly enriched relatively to the Upper Continental Crust (UCC) in the FA, FB1a, FB1b, FB2a, and FB2b (< 3) while it is moderately enriched in the FB1c unit and the FD Formation (> 3) and sometimes strongly enriched (> 10) in the FC Formation. The enrichment of As in these units is due to syngenetic hydrothermal input (Fig. 1a).

4- Paleo-weathering conditions

CIA average values were around 70% for FB1b, FC, and FD (71.9 %, 70.1 % and 72.5 %, respectively), 75.9 % for the FB1a and around 85 % for the FA, FB1c, FB2a and FB2b (85.5 %, 85.9 %, 85.3 % and 85.4 %, respectively) samples (Fig. 1d). According to CIA values, the FA rocks are highly weathered (>80 %)[12]. This value decreases progressively into the FB1a and FB1b units to reach values of moderately weathered rocks (60-80 %). Then average CIA values increase again into highly weathered rocks until the FB2b unit. The FC and FD formations show a decrease in weathering intensity, indicating moderately weathered rocks.

As normalized to detrital proxies (Al and Ti) (Fig. 1b, 1c) follows identical trends and it suggests, when combined with CIA values (Fig. 1b), that most of the As in the basin originated from continental weathering marked by variations in chemical weathering when CIA values are high and mechanical weathering when the values are low. These results are in agreement with previous findings[9,11,13] based on Fe speciation and trace metal enrichment in the different units of the Francevillian Series. Arsenic is enriched in anoxic/euxinic units and depleted in oxic conditions. In fact, redox conditions varied across the section with bottom-water oxic conditions mainly established in the lower part of the section (FB1a unit) and then switched to bottom-water anoxic conditions under a hydrothermal influence in the FB1c ferruginous/manganous unit.

5- Evidence of arsenic cycling in Phanerozoic metazoans and implications

Arsenic accumulations in eukaryotic cells, evident in some of the oldest known examples of multicellular life (Figs. S6, S7, S8), suggest that metabolisms capable of coping with metalloid stress were present early in the eukaryotic evolution, at least since 2.1 billion years ago. This could explain why such metabolisms and associated processes are widespread across all branches of the eukaryotic tree of life, including arthropods, echinoderms, and mammals[14]. To fully understand the evolutionary trajectory of these metabolisms, it is essential to investigate arsenic concentrations not only in early eukaryotes (as examined in this study) and modern animals[15–17] but also to bridge the gap between these ancient organisms and modern eumetazoans by studying intermediate life forms from the Phanerozoic.

An investigation of arthropods such as *Coeloma rupeliense*[18], (Decapoda, Bilzen formation, Belgium, Rupelian) (Fig. S6) and *Penaeoidea indet*[19] (Decapoda, La Voulte sur Rhône, France, Callovian) (Fig. S7) revealed that arsenic is associated with small pyrite grains. Arsenic-bearing pyrite was observed in numerous fossils from the Cambrian Walcott Quarry[20–22] (Burgess Shale, Canada), including marellomorphs (Fig. S8a) where arsenic is associated with sulfur, iron, and nickel particularly in the gut (Fig. S8b-e), and at a smaller scale, formed a nucleus inside micro-pyrite (Fig. S8f- j), and echinoderms from the Hunsrück Slate[23] (Devonian, Germany) (Fig. S8k) where arsenic is found in association with pyrite (i.e., see correlation between sulfur and arsenic), primarily associated with the digestive gland, and sometimes with the skeleton (Fig. S8l-q). The pyrite in these fossils precipitated early during diagenesis, replicating anatomical details with remarkable precision[24]. This occurred regardless of whether pyrite was the primary preservation mode, as in the Hunsrück Slate[25], or an accessory preservation mode, as in the Burgess Shale, where carbonaceous compressions dominate[26–28]. Pyrite formed during early diagenesis while carcasses decayed increasing the resistance of biological tissues over geological times[29–31]. Despite contrasting late diagenetic, metamorphic, and weathering histories of the investigated Phanerozoic eumetazoan fossils[24,32–35], there is some similarity in arsenic distribution across samples (Figs. S6, S7) suggesting a potential bioaccumulation of arsenic homologous to the Gabonese fossils. This aligns with observations of arsenic storage in the tissues of numerous modern organisms such as fishes, rats, and felids[36–38]. Thus, the process of arsenic storage in cells likely began at least 2.1 billion years ago, early in eukaryotic evolution, and became widespread through the Cambrian diversification of eumetazoans.

Supplementary figures

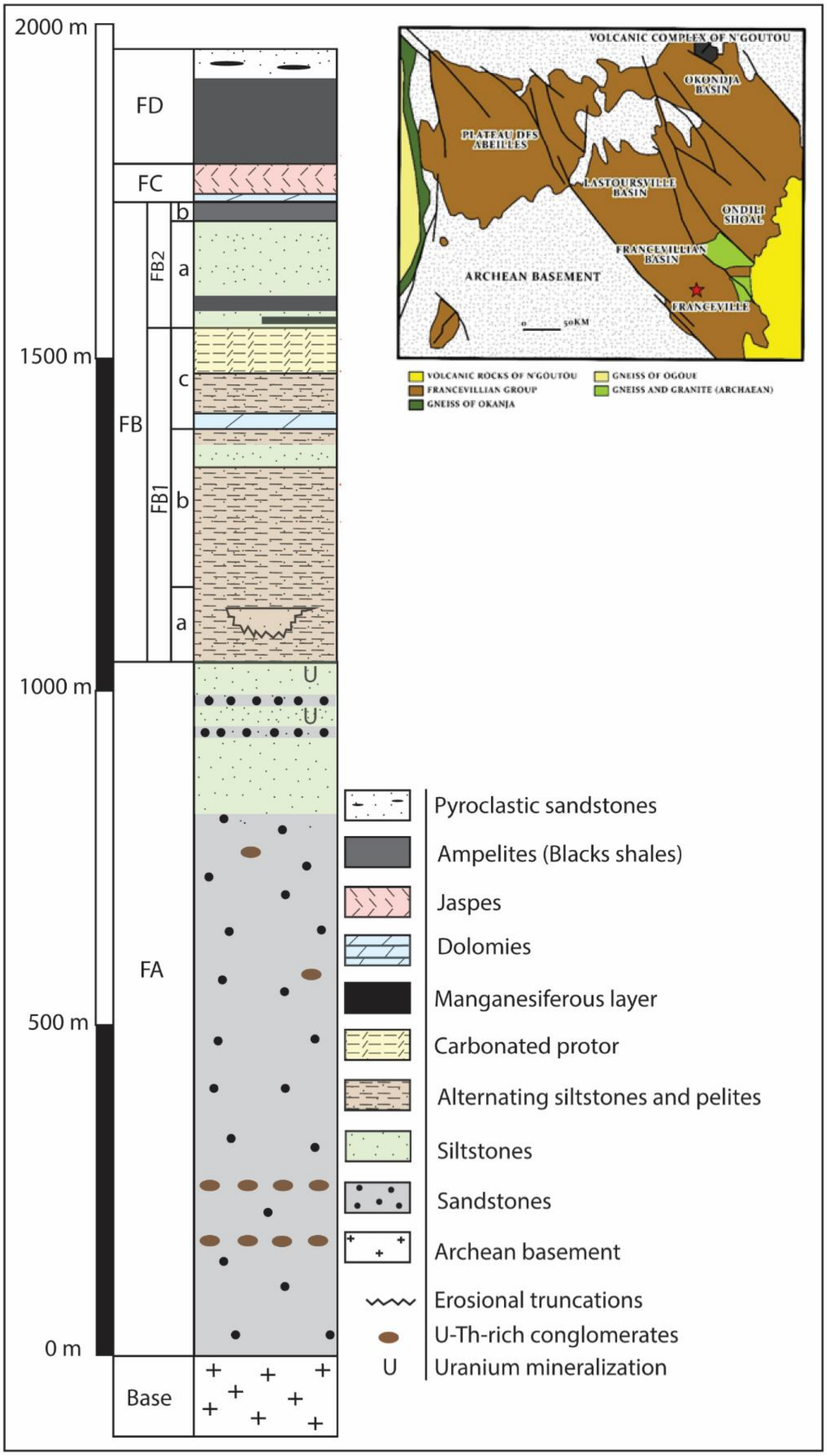

Figure. S1: Geological map and stratigraphic section of the Francevillian Group (modified from Ikouanga et al., 2024[39]).

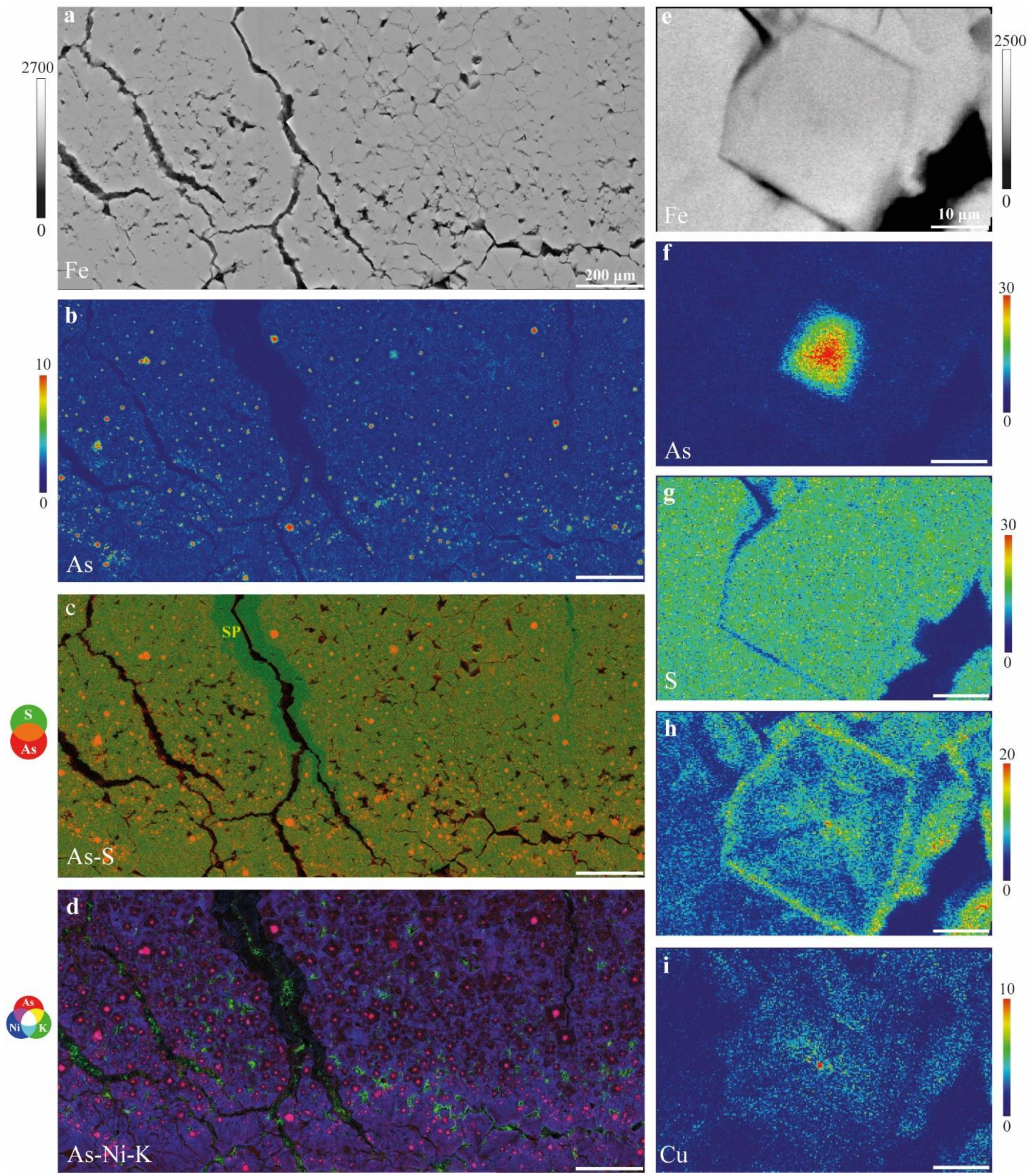

Figure. S2 X-Ray fluorescence (XRF) imaging of elongate fossils. a, Nano-X-ray fluorescence (XRF) elemental map of Fe in an elongate fossil shows coagulated pyrite. The distribution of As (**b**) and As-S co-localization (**c**) shows a concentric As distribution within pyrite grains with secondary pyrite (SP) near the porosity. **d**, The distribution of As, Ni and K shows As zonation and association with Ni in pyrite grains found in a clay-rich matrix. Pixel size of (a-d) is 1µm. Distribution of Fe (**e**), S (**f**), As (**g**), Ni (**h**) and Cu (**i**) within a pyrite grain measured with 150 nm resolution shows As nuclei in association with Ni and Cu.

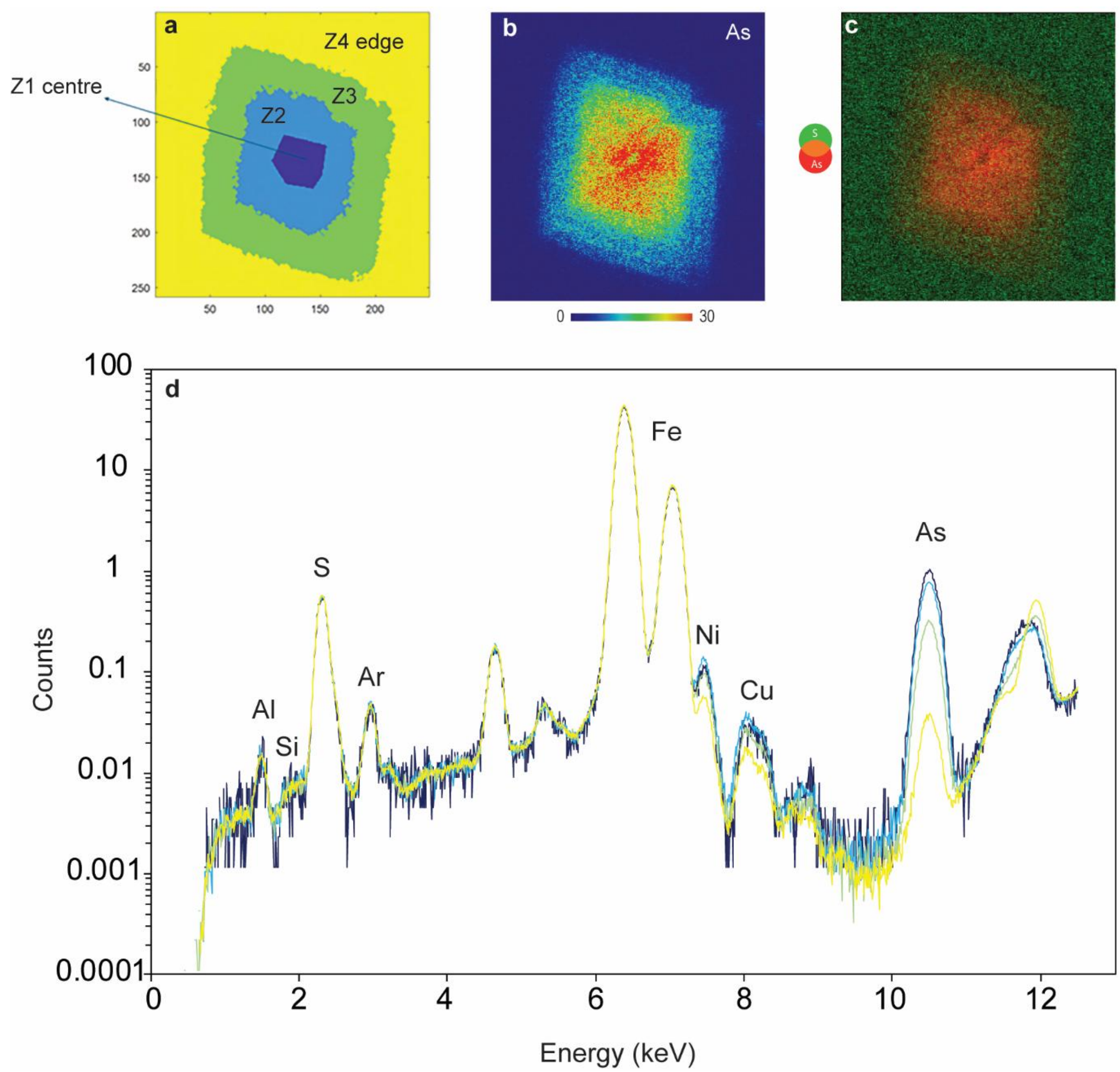

Figure. S3 Mean X-Ray Fluorescence (XRF) spectra of different zones of a pyrite crystal from a tubular fossil. The zones (Z1, Z2, Z3 and Z4) were defined in the function of the arsenic content within the pyrite crystal (**a**,**b**,**c**). The colors of the XRF spectra (**d**) correspond to the zones shown in (**a**) and they represent the mean XRF spectra of a pixel (150 nm^2) in 20 ms dwell time.

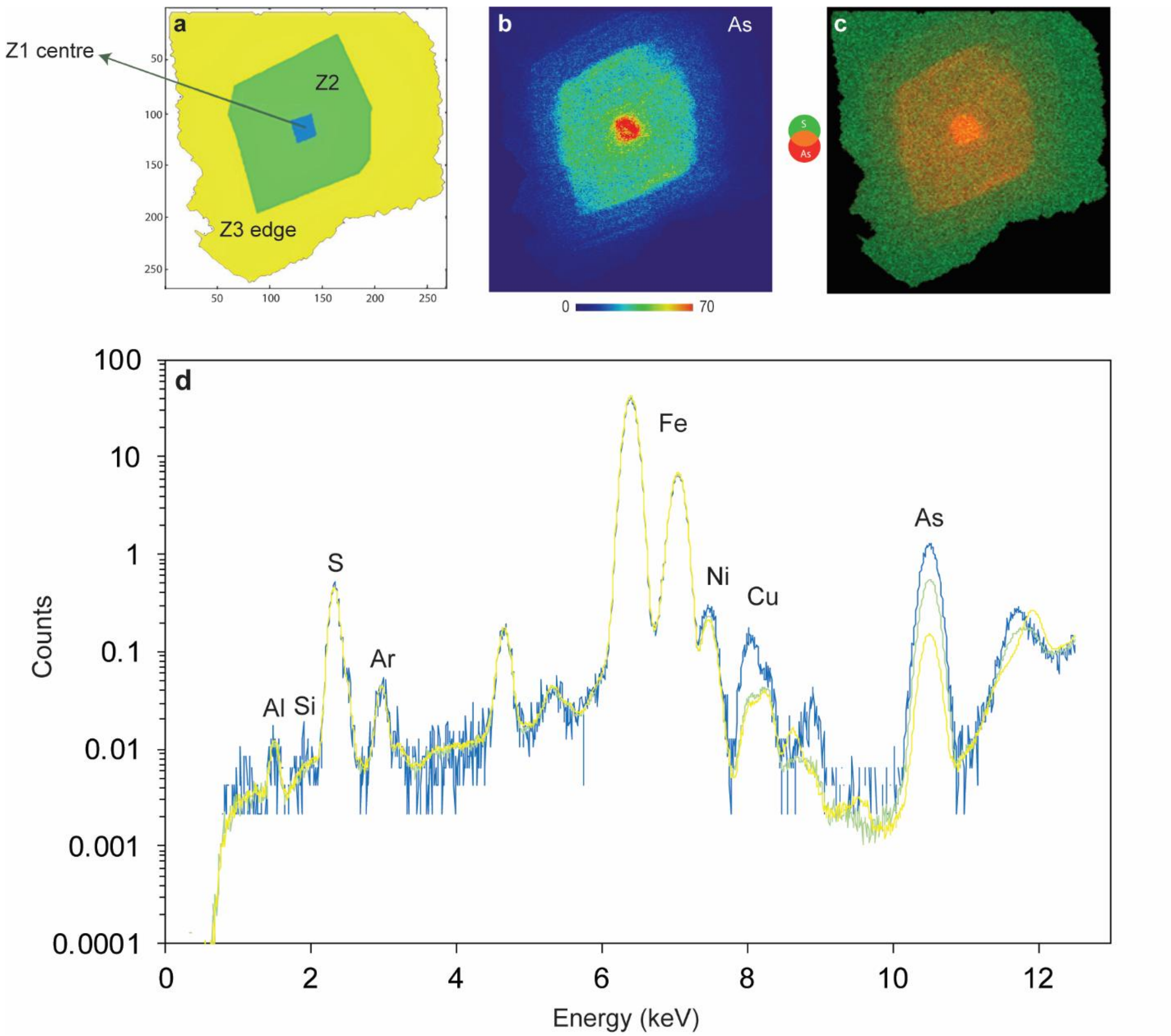

Figure. S4 Mean X-Ray Fluorescence (XRF) spectra of different zones of a pyrite crystal from a lobate fossil. The zones (Z1, Z2 and Z3) were defined in the function of the arsenic content within the pyrite crystal (**a**,**b**,**c**). The colors of the XRF spectra (**d**) correspond to the zones shown in (**a**) and they represent the mean XRF spectra of a pixel (150 nm^2) in 20 ms dwell time.

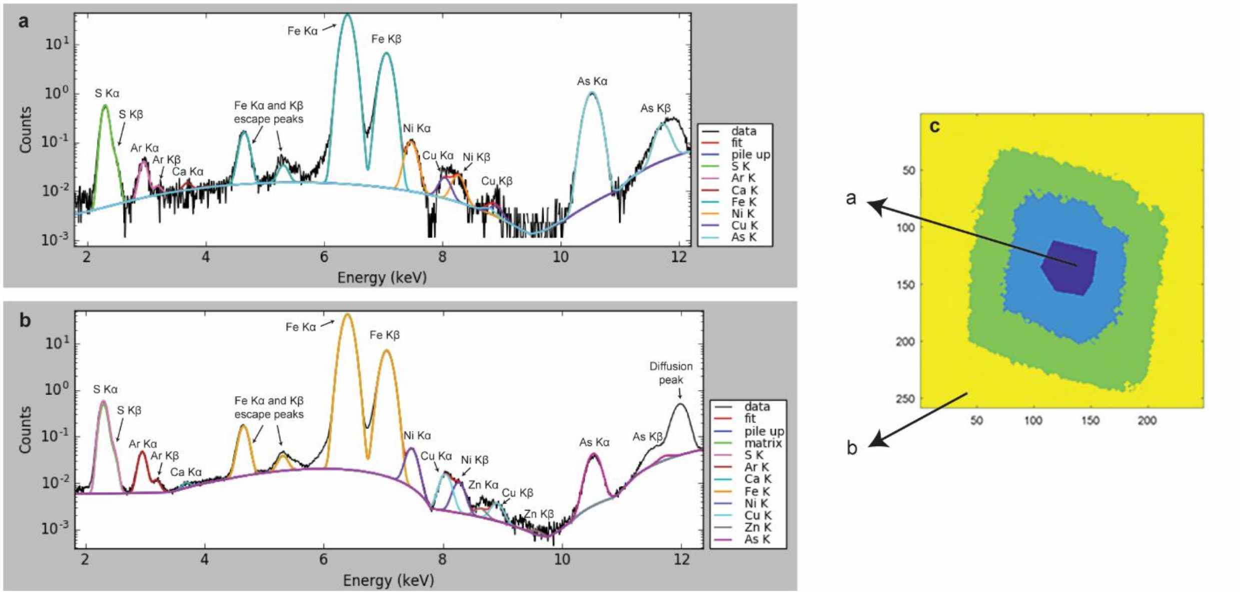

Figure. S5 Deconvolution of mean X-Ray Fluorescence (XRF) spectra for a tubular fossil's pyrite grain shown in figure. S3. The deconvolution of the mean XRF spectra has been performed by PyMCA. The identified elements, peak-overlapping, spectral artifact (e.g. Fe escape peaks), background corrections and pile-up (negligible in the spectral zone of interest) can be seen in the central (**a**) and side (**b**) zones of the single pyrite crystal. (**c**, see also figure. S3).

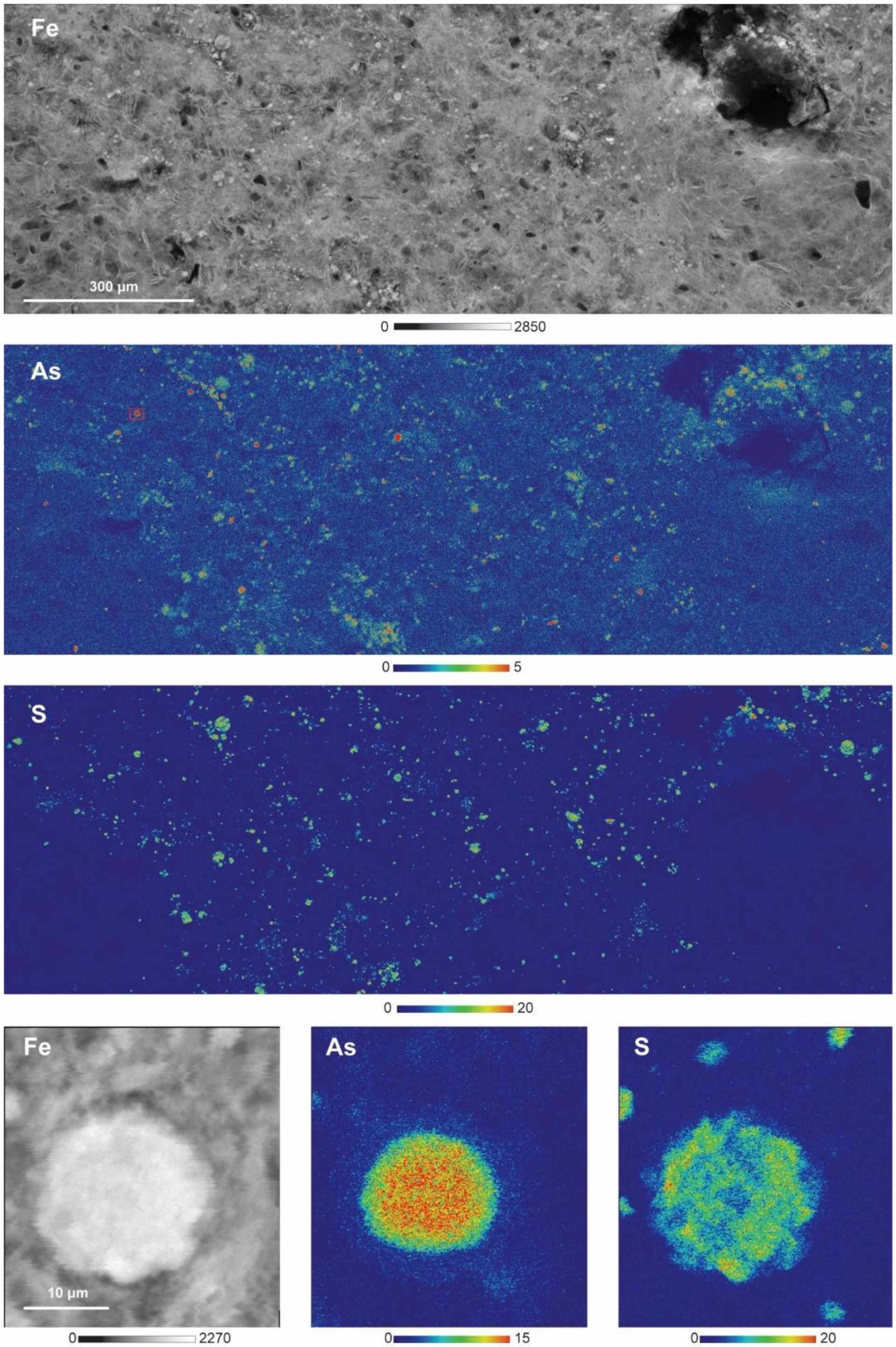

Figure. S6 Arsenic zonation in micro-pyrite Nano-XRF elemental mapping of Fe, As and S and a zoom on one pyrite grain with 150 nm pixel size (red rectangle) in a *Coeloma rupeliense* specimen shows As correlation and zonation in micro-pyrite. The pixel size of upper Fe, As, and S maps is 1µm.

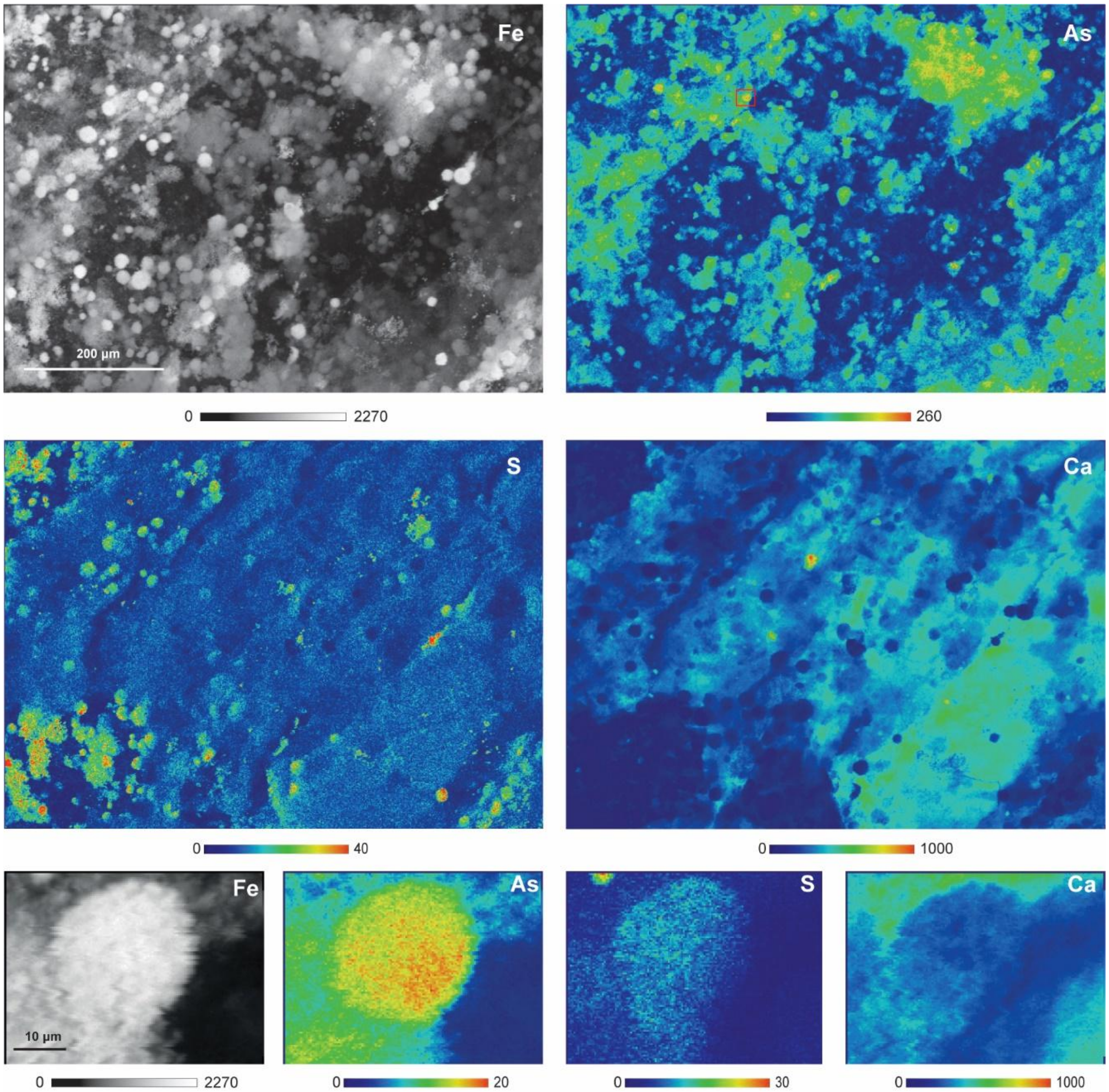

Figure. S7 Arsenic zonation in micro-pyrite Nano-XRF elemental mapping of Fe, As and S and Ca and a zoom on one pyrite grain with 150 nm pixel size (red rectangle) in a *Penaeoidea indet* specimen shows As correlation and zonation in micro-pyrite. The pixel size of upper Fe, As, and S maps is 1 µm.

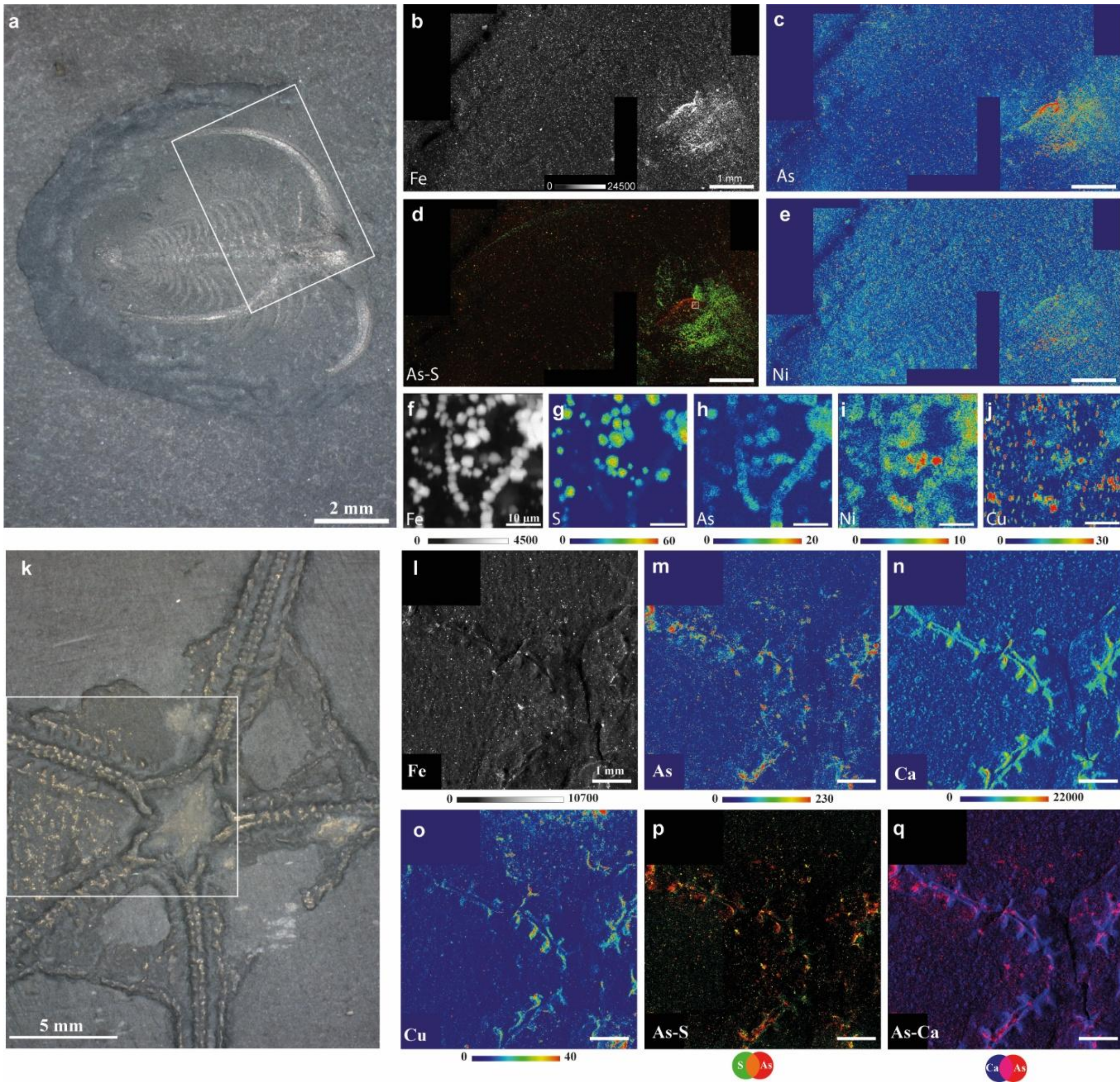

Figure. S8 Arsenic enrichment in exceptionally preserved Phanerozoic fossils. **a**, an optical microscope image of *Marella* specimen from the Cambrian Walcott Quarry. The white rectangle represents the analyzed area. Nano- x-ray fluorescence (Nano-XRF) elemental mapping of iron (**b**), arsenic (**c**), sulfur (**d**) and nickel (**e**), illustrating a high concentration of these elements in the gut. Elemental mapping of iron (**f**), sulfur (**g**), arsenic (**h**), nickel (**i**), and copper (**j**) on a magnified area of the gut showing arsenic zonation with sulfur and nickel inside micro-pyrites and dispersed copper hotspots. **k**, An optical microscope image of an echinoderm from the Hunsrück Slate. The white indicates the analyzed area. **l**, Nano-XRF elemental mapping of iron shows the presence of micro-pyrite. Nano-XRF elemental mapping showing arsenic (**m**) in the digestive glands and skeletonized calcium (**n**) and copper (**o**). Nano-XRF elemental mapping showing arsenic associating mainly with sulfur (**p**) and calcium (**q**). The pixel size of (b-e) and (l-q) is 5 µm, and that of (f-j) is 150 nm.

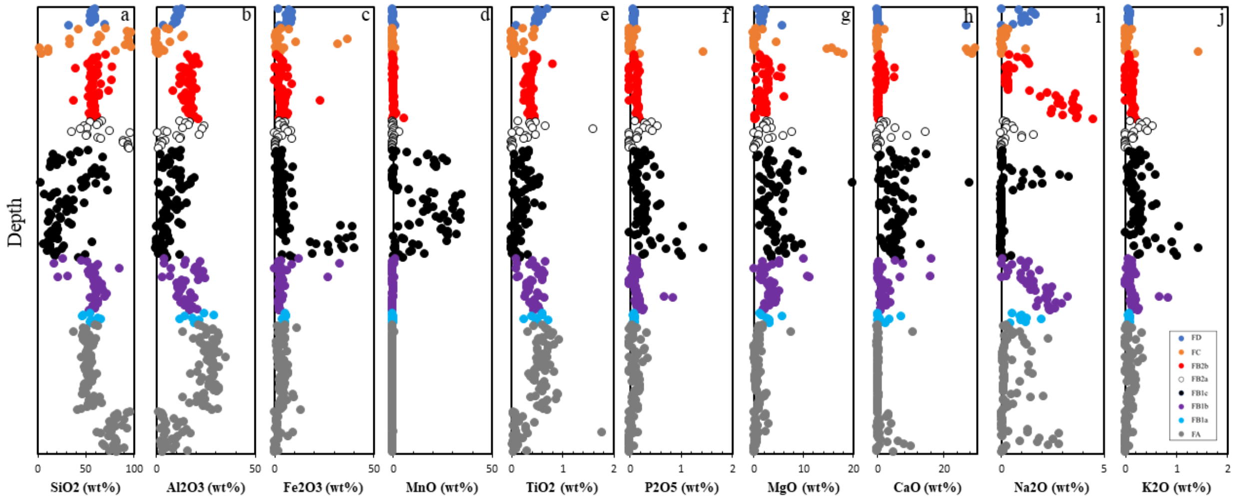

Figure. S9 Major elements wt% across the different units of the Francevillian section a, SiO_2,, **b**, Al_2O_3,, **c**, Fe_2O_3,, **d**, MnO, **e**, TiO_2,, **f**, P_2O_5, **g**, MgO, **h**, CaO, **I**, Na_2O, **j**, K_2O.

References

1. Weber, F. Sédimentologie, géochimie, relations avec les gites minéraux associés. (1968).
2. Bankole, O. M., El Albani, A., Meunier, A. & Gauthier-Lafaye, F. Textural and paleo-fluid flow control on diagenesis in the Paleoproterozoic Franceville Basin, South Eastern, Gabon. *Precambrian Research* **268**, 115–134 (2015).
3. Gauthier-Lafaye, F., Holliger, P. & Blanc, P.-L. Natural fission reactors in the Franceville basin, Gabon: A review of the conditions and results of a "critical event" in a geologic system. *Geochimica et Cosmochimica Acta* **60**, 4831–4852 (1996).
4. Ikouanga, J. N. *et al.* Taphonomy of early life (2.1 Ga) in the francevillian basin (Gabon): Role of organic mineral interactions. *Precambrian Research* **395**, 107155 (2023).
5. Bankole, O. M., El Albani, A., Meunier, A., Poujol, M. & Bekker, A. Elemental geochemistry and Nd isotope constraints on the provenance of the basal siliciclastic succession of the middle Paleoproterozoic Francevillian Group, Gabon. *Precambrian Research* **348**, 105874 (2020).
6. Gauthier-Lafaye, F. & Weber, F. The Francevillian (Lower Proterozoic) uranium ore deposits of Gabon. *Economic Geology* **84**, 2267–2285 (1989).
7. Reynaud, J.-Y. *et al.* Depositional setting of the 2·1 Ga Francevillian macrobiota (Gabon): Rapid mud settling in a shallow basin swept by high-density sand flows. *Sedimentology* **65**, 670–701 (2018).
8. El Albani, A. *et al.* The 2.1 Ga Old Francevillian Biota: Biogenicity, Taphonomy and Biodiversity. *PLoS ONE* **9**, e99438 (2014).
9. Canfield, D. E. *et al.* Oxygen dynamics in the aftermath of the Great Oxidation of Earth's atmosphere. *Proc. Natl. Acad. Sci. U.S.A.* **110**, 16736–16741 (2013).
10. Bertrand-Sarfati, J. & Potin, B. Microfossiliferous cherty stromatolites in the 2000 Ma Franceville Group, Gabon. *Precambrian Research* **65**, 341–356 (1994).
11. Chi Fru, E. *et al.* Hydrothermal seawater eutrophication triggered local macrobiological experimentation in the 2100 Ma Paleoproterozoic Francevillian sub-basin. *Precambrian Research* **409**, 107453 (2024).
12. Fedo, C. Unraveling the effects of potassium metasomatism in sedimentary rocks and paleosols, with implications for paleoweathering conditions and provenance. (1995).
13. El Albani, A. *et al.* Organism motility in an oxygenated shallow-marine environment 2.1 billion years ago. *Proc. Natl. Acad. Sci. U.S.A.* **116**, 3431–3436 (2019).
14. Sánchez-Bayo, F. Ecological Impacts of Toxic Chemicals.
15. Aposhian, H. V. *et al.* How is Inorganic Arsenic Detoxified? in *Arsenic Exposure and Health Effects III* 289–297 (Elsevier, 1999). doi:10.1016/B978-008043648-7/50033-9.
16. Mogren, C. L., Von Kiparski, G. R., Parker, D. R. & Trumble, J. T. Survival, reproduction, and arsenic body burdens in Chironomus riparius exposed to arsenate and phosphate. *Science of The Total Environment* **425**, 60–65 (2012).
17. Choi, J. Y. *et al.* Determination of toxic heavy metals in Echinodermata and Chordata species from South Korea. *Food Additives & Contaminants: Part B* **7**, 295–301 (2014).
18. Jagt, J. W. M. Coeloma rupeliense (Crustacea, Decapoda, Brachyura) from the Bilzen Formation (Rupel Group, Lower Oligocène) in northeast Belgium.
19. Jauvion, C., Charbonnier, S. & Bernard, S. A new look at the shrimps (Crustacea, Decapoda, Penaeoidea) from the Middle Jurassic La Voulte-sur-Rhône Lagerstätte. *Geodiversitas* **39**, 705–716 (2017).
20. Butterfield, N. J. Organic preservation of non-mineralizing organisms and the taphonomy of the Burgess Shale. *Paleobiology* **16**, 272–286 (1990).

21. Butterfield, N. J. Secular distribution of Burgess-Shale-type preservation. *LET* **28**, 1–13 (1995).
22. Butterfield, N. J., Balthasar, U. & Wilson, L. A. Fossil diagenesis in the Burgess Shale. *Palaeontology* **50**, 537–543 (2007).
23. Clark, E. G., Hutchinson, J. R. & Briggs, D. E. G. Three-dimensional visualization as a tool for interpreting locomotion strategies in ophiuroids from the Devonian Hunsrück Slate. *R. Soc. open sci.* **7**, 201380 (2020).
24. Farrell, Ú. C. Pyritization of Soft Tissues in the Fossil Record: An Overview. *Paleontol. Soc. pap.* **20**, 35–58 (2014).
25. Tibbs, S. L., Briggs, D. G. & Prossl, K. F. Pyritisation of plant microfossils from the Devonian Hunsriick Slate of Germany.
26. Gaines, R. R., Briggs, D. E. G. & Yuanlong, Z. Cambrian Burgess Shale–type deposits share a common mode of fossilization. *Geol* **36**, 755 (2008).
27. Gaines, R. R. *et al.* Mechanism for Burgess Shale-type preservation. *Proc. Natl. Acad. Sci. U.S.A.* **109**, 5180–5184 (2012).
28. Saleh, F. *et al.* Insights into soft-part preservation from the Early Ordovician Fezouata Biota. *Earth-Science Reviews* **213**, 103464 (2021).
29. Saleh, F., Daley, A. C., Lefebvre, B., Pittet, B. & Perrillat, J. P. Biogenic Iron Preserves Structures during Fossilization: A Hypothesis: Iron from Decaying Tissues May Stabilize Their Morphology in the Fossil Record. *BioEssays* **42**, 1900243 (2020).
30. Gabbott, S. E., Xian-guang, H., Norry, M. J. & Siveter, D. J. Preservation of Early Cambrian animals of the Chengjiang biota. *Geol* **32**, 901 (2004).
31. Guan, C. *et al.* Controls on fossil pyritization: Redox conditions, sedimentary organic matter content, and Chuaria preservation in the Ediacaran Lantian Biota. *Palaeogeography, Palaeoclimatology, Palaeoecology* **474**, 26–35 (2017).
32. Topper, T. P., Greco, F., Hofmann, A., Beeby, A. & Harper, D. A. T. Characterization of kerogenous films and taphonomic modes of the Sirius Passet Lagerstätte, Greenland. *Geology* **46**, 359–362 (2018).
33. Jauvion, C. *et al.* Exceptional preservation requires fast biodegradation: thylacocephalan specimens from La Voulte-sur-Rhône (Callovian, Jurassic, France). *Palaeontology* **63**, 395–413 (2020).
34. Anderson, R. P., Tosca, N. J., Saupe, E. E., Wade, J. & Briggs, D. E. G. Early formation and taphonomic significance of kaolinite associated with Burgess Shale fossils. *Geology* **49**, 355–359 (2021).
35. Staatliches Museum für Naturkunde Karlsruhe, Kimmig, J. & Schiffbauer, J. Finding and describing the exceptional: a modern definition of fossil-lagerstätten. in 392647 (2023). doi:10.1130/abs/2023AM-392647.
36. Alborough, R. *et al.* Renal accumulation of prooxidant mineral elements and CKD in domestic cats. *Sci Rep* **10**, 3160 (2020).
37. Ferreira, N. D. S. *et al.* Arsenic bioaccumulation and biotransformation in different tissues of Nile tilapia (Oreochromis niloticus): A comparative study between As(III) and As(V) exposure and evaluation of antagonistic effects of selenium. *Chemosphere* **359**, 142289 (2024).
38. Coimbra, J. L. P. *et al.* Subchronic intake of arsenic at environmentally relevant concentrations causes histological lesions and oxidative stress in the prostate of adult Wistar rats. *Reproductive Toxicology* **128**, 108647 (2024).

39. Ikouanga, J. N. *et al.* The first application of Re–Os dating on Paleoproterozoic Francevillian sediments (Gabon). *Comptes Rendus. Géoscience* **356**, 57–66 (2024).